# On-sky operations and performance of LMIRcam at the Large Binocular Telescope

J. M. Leisenring[a], M. F. Skrutskie[b], P. M. Hinz[c], A. Skemer[c], V. Bailey[c], J. Eisner[c],
P. Garnavich[d], W. F. Hoffmann[c], T. Jones[e], M. Kenworthy[f], P. Kuzmenko[g], M. Meyer[a],
M. Nelson[b], T. J. Rodigas[c], J. C. Wilson[b], V. Vaitheeswaran[c]

[a]ETH Zürich, Wolfgang-Pauli-Strasse 27, 8093, Züich, Switzerland;
[b]University of Virginia, 530 McCormick Rd, Charlottesville, VA, 22904, USA;
[c]Steward Observatory, University of Arizona, 933 N. Cherry Ave, Tucson, AZ, 85721, USA;
[d]University of Notre Dame, 225 Nieuwland Science, Notre Dame, IN, 46556, USA;
[e]University of Minnesota, 116 Church St SE, Minneapolis, NM, 55455, USA;
[f]Leiden Observatory, Leiden University, P.O. Box 9513, 2300 RA Leiden, The Netherlands;
[g]Lawrence Livermore National Laboratory, 7000 East Avenue, Livermore, CA 94550, USA

## ABSTRACT

The $L/M$-band ($3-5$ $\mu$m) InfraRed Camera (LMIRcam) sits at the combined focal plane of the Large Binocular Telescope Interferometer (LBTI), ultimately imaging the coherently combined focus of the LBT's two 8.4-meter mirrors. LMIRcam achieved first light at the LBT in May 2011 using a single AO-enabled 8.4-meter aperture. With the delivery of LBT's final adaptive secondary mirror in Fall of 2011, dual-aperture AO-corrected interferometric fringes were realized in April 2012. We report on the performance of these configurations and characterize the noise performance of LMIRcam's HAWAII-2RG 5.3-$\mu$m cutoff array paired with Cornell FORCAST readout electronics. In addition, we describe recent science highlights and discuss future improvements to the LMIRcam hardware.

**Keywords:** Infrared, Interferometry, Fizeau, HgCdTe detectors

## 1. INSTRUMENT OVERVIEW

Developed through a collaboration between the Universities of Arizona, Minnesota, Notre Dame, and Virginia, the $L/M$-band InfraRed camera (LMIRcam) was designed to perform imaging and spectroscopy within the $L$ (3.6 $\mu$m) and $M$ (4.8 $\mu$m) atmospheric windows while taking full advantage of the diffraction-limited Fizeau interferometry unique to the Large Binocular Telescope (LBT). LMIRcam's wavelength coverage fills a niche amongst such instruments designed to re-image the combined light from the LBT's two telescopes, fitting midway between that of LINC-NIRVANA[1] ($1-2.5$ $\mu$m) and the Nulling Optimized Mid-Infrared Camera[2] (NOMIC; $8-13$ $\mu$m).

As of May 2011, LMIRcam operates behind the NASA-funded LBT Interferometer (LBTI),[3] which coherently combines the beams from the two 8.4-meter mirrors. The LBTI serves as the beam combiner for both LMIRcam and NOMIC, which share the same cryostat collectively known as the Nulling and Imaging Camera (NIC). Due to its fixed baseline, the LBTI successfully delivers a PSF over a wide field of view that is the modulation of an 8.4-meter Airy pattern with a 2-slit diffraction pattern along the direction of the two-telescope baseline. The NIC cryostat also houses a $K$-band fast readout camera (Phasecam) to sense phase variations between the LBT apertures and carry out closed-loop correction. Within the operational wavelength range of LMIRcam, LBTI's first interferometric null lies at a distance of approximately 30 mas from the image centroid. LMIRcam re-images the LBTI focal plane at a 1:1 ratio onto a 1024×1024 HgCdTe detector, providing a $10'' \times 10''$ FOV and a 10.9 mas/pixel plate scale (Nyquist sampling or better of the interferometrically diffracted PSFs). However, the optical design can accommodate an unvignetted 2048×2048 array. Wilson et al. (2008)[4] and Skrutskie et al. (2010)[5] provide extensive details on the design of LMIRcam's optical and mechanical layout.

Two biconic mirrors and three fold mirrors provide two intermediate pupils for filters and grisms as well as an intermediate focal plane. A total of two filter box assemblies, each containing two filter wheels, sit at

Ground-based and Airborne Instrumentation for Astronomy IV, edited by Ian S. McLean, Suzanne K. Ramsay,
Hideki Takami, Proc. of SPIE Vol. 8446, 84464F · © 2012 SPIE · CCC code: 0277-786X/12/$18 · doi: 10.1117/12.924814

Downloaded From: http://proceedings.spiedigitallibrary.org/ on 02/01/2013 Terms of Use: http://spiedl.org/terms

**Table 1. LMIRcam Operational Specifications**

| **Specification** | ***L*-band** | ***M*-band** | **Units** |
|---|---|---|---|
| Wavelength Coverage | 3.4 – 4.0 | 4.6 – 5.0 | $\mu$m |
| Single-Aperture Resolution | 90 | 120 | mas |
| Dual-Aperture Resolution | 26 | 34 | mas |
| Spectral Resolution | $R \sim 300$ | | – |
| Pixel Scale | 10.9 | | mas/pixel |
| Field of View | 10×10 | | arcsec |
| Estimated Strehl | 90 | 95 | % |
| Background Sensitivity | 7 | 70 | $\mu$Jy |
| (5-$\sigma$ in 1 hour of integration) | 19.0 | 15.8 | mag |

the intermediate pupil planes, while a single aperture wheel sits at the intermediate focal plane. With twelve positions per filter wheel, this layout offers a number of possible operating configurations. The first wheel exclusively holds pupil masks and coronagraphic components, while numerous narrow and broadband filters are populated throughout the rest of the wheels. The wheel nearest to the detector holds grisms with the respective slit masks positioned within an intermediate focal plane at the aperture wheel.

This manuscript presents the on-sky performance analysis of LMIRcam based on data collected during commissioning and engineering time in April 2012. We begin by highlighting the various instrument observing modes (e.g., single-aperture AO, dual-aperture interferometry, grism spectroscopy, phase apodizing coronagraphy, and non-redundant masking) and continue by presenting an update on the state of LMIRcam's electronics subsystem. Finally, we briefly discuss recent science results as well as plans for near-future hardware upgrades.

**Table 2. Filter and Aperture Wheels**

| **Pos** | **Wheel 1** | **Wheel 2** | **Field Stop** | **Wheel 3** | **Wheel 4** |
|---|---|---|---|---|---|
| 1 | Open | Open | Open | Open | Open |
| 2 | Small Dual Ap[a] | N0304-016 | 0.34-mm Slit | Open | PK-50 Blocker |
| 3 | Large Dual Ap[a] | N0317-007 | 0.17-mm Slit | Open | *L*-Grism 1[f] |
| 4 | DX Aperture[b] | N0331-016 | 0.25-mm Pinhole | Open | *L*-Grism 2[f] |
| 5 | SX Aperture[b] | N0347-015 | – | W0331-041 | *M*-Grism 1[f] |
| 6 | 24-hole NRM[c] | N0359-009 | – | W0370-058 | *M*-Grism 2[f] |
| 7 | 12-hold NRM[c] | N0378-020 | – | W0479-037 | N0308-014 |
| 8 | Annulus NRM[c] | N0395-023 | – | W0341-119 | N0406-007 |
| 9 | Positive APPs[d] | ND (T=10%) | – | Open | N0401-007 |
| 10 | Negative APPs[d] | ND (T=1%) | – | N0329-005 | W0378-055 |
| 11 | 0.33-mm Pinhole | SX Half-moon[e] | – | N0341-005 | W0523-125 |
| 12 | Blank | DX Half-moon[e] | – | Blank | Pupil Imaging Lens |

---

[a] Undersized and oversized pupil masks for simultaneous imaging of the two telescope beams

[b] Pupil masks for imaging either the right or left beam

[c] Non-redundant masks

[d] Apodized phase plates, each holding a separate optic per telescope beam

[e] Masks for blocking either the right or left beam for any dual-aperture pupil configuration

[f] Two grisms were manufactured for each band in order to orient the dispersion parallel or perpendicular to the interferometric axis

Downloaded From: http://proceedings.spiedigitallibrary.org/ on 02/01/2013 Terms of Use: http://spiedl.org/terms

## 2. OBSERVING MODES

There are many elements within the LBT framework that contribute towards realizing AO-corrected dual-apeture interferometry imaged at the LMIRcam focal plane.[6] The LBTI ultimately takes advantage of the high performance of the LBT's First Light AO (FLAO) system[7] in order to produce an interferometric PSF with a two-slit diffraction pattern along the baseline of the two telescopes. This system has been brought up in stages with the first of two adaptive secondary mirrors installed in Spring 2010. LMIRcam was subsequently commissioned during May 2011 utilizing only this installed AO system. The final adaptive secondary began installation in August 2011, allowing for dual-aperture AO-corrected interferometric observations with LMIRcam during an engineering run in April 2012.

In addition to simple imaging, LMIRcam is equipped with various observing modes, including dispersive grisms, apodized phase plates, and non-redundant masks. Table 2 summarizes these optical components along with the current complement of filters as they are positioned within the LMIRam cryogenic filter and aperture boxes. Filter names beginning with 'N' refer to narrowband while 'W' indicates a wideband (or broadband) filter. The first four digits correspond to central wavelength of the filter (i.e., '0304' = 3.04 $\mu$m), and the last three digits correspond to the width of the filter's band (i.e., '016' = 0.16 $\mu$m). The twelve-position wheels located near the intermediate pupil planes provide ample room for future expansion and flexibility to combine various observing modes.

### 2.1 Steps Towards Dual-Aperture Interferometry

Producing interferometric fringes with LMIRcam is a multistep process, which involves: 1) independently locking and tuning the target star on each of the two AO systems; 2) spatially overlapping the two images at the detector focal plane; and 3) minimizing the path length difference between the two beams in order to coherently combine the light and obtain an interferometric PSF. The final product provides a PSF more centrally concentrated with a smaller footprint compared to the traditional Airy pattern. As a result, this configuration improves the contrast limit for detecting faint objects at close angular separations to a bright source due to the relative 'peakiness' of both objects' PSFs. In particular, light from the primary source becomes easier to remove at a given distance, and the faint source appears brighter because the light is less extended.

When a star is initially acquired, the two telescope beams produce separate images at arbitrary spatial locations on the detector plane. In principle, the LBT's two apertures can be operated independently of each other and act as two separate 8.4-meter telescopes. The LBTI beam combiner can choose to image either the right or the left aperture by themselves or both at the same time. Similarly, pupil plane masks within LMIRcam's

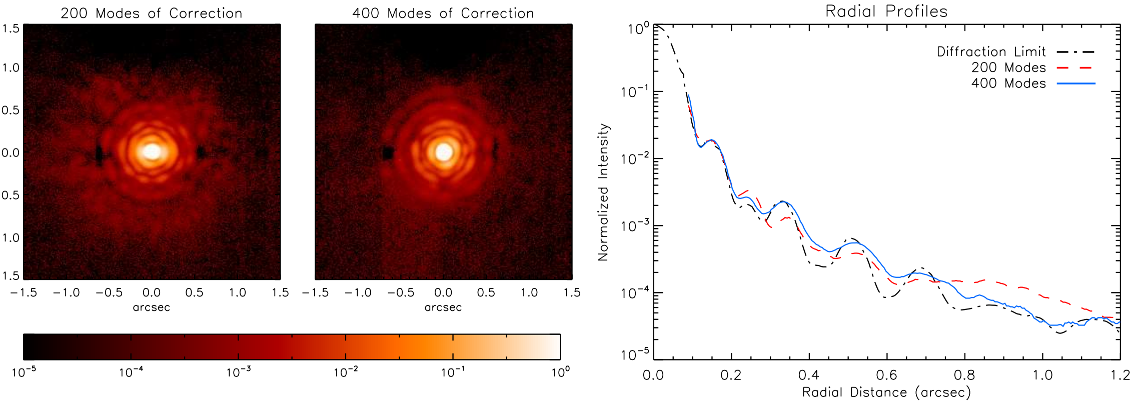

Figure 1. *Left*: AO-corrected $L'$-Band images of a bright star ($R = 5.2$, $L' = 3.9$) under moderate seeing conditions ($\sim 1.6''$) using 200 (left) and 400 (right) modes of correction. Total integration time is approximately 30 sec. Due to the bright nature of this source, the PSF core is saturated and evidence of channel crosstalk can be observed as dark spots on either side of the PSFs (approximately 64 pixels away to the left and right). *Right*: Plots of the radial profiles of the two PSFs compared to the diffraction limited case from Esposito et al. (2011),[7] which has been scaled to LMIRcam's wavelength of $\lambda = 3.8$ $\mu$m. The observed LMIRcam PSFs have further been normalized such that the unsaturated region in the core and first Airy ring matches that of the diffraction-limited PSF.

Downloaded From: http://proceedings.spiedigitallibrary.org/ on 02/01/2013 Terms of Use: http://spiedl.org/terms

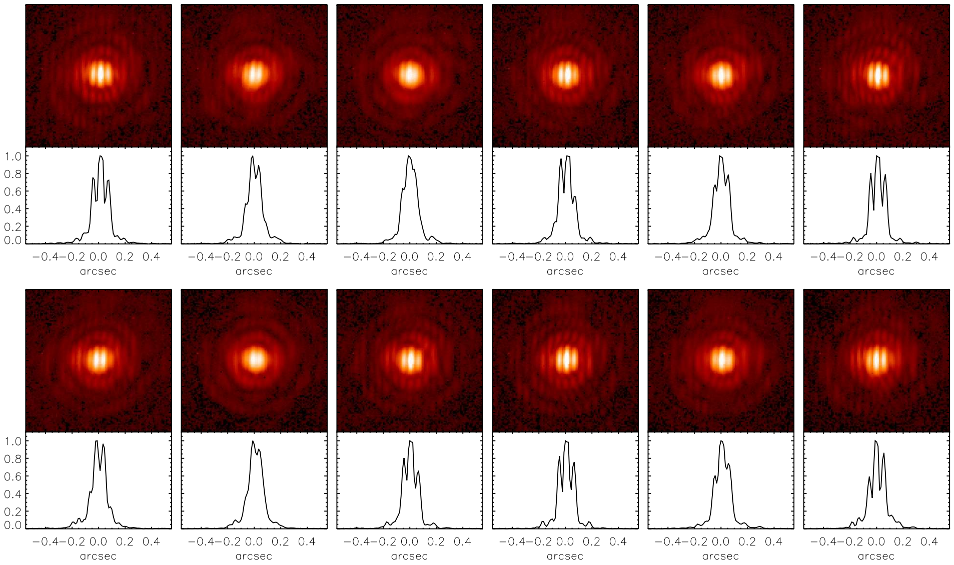

Figure 2. Time series of interferometric images in a narrowband filter at ~4 $\mu$m of a bright source ($R = 2.2$, $L = -1.3$) showing the phase stability in a power-law stretch. Below each image is a plot of the relative intensities of a cross-sectional cut at $Y = 0$. The core of the PSFs are saturated in this case, which reduces the observed contrast between the peak value and the interferometric nulls. Integration time per frame was set at 87 msec with a frame acquisition rate of ~5Hz.

filter wheels provide the ability to switch off either the DX (right) or SX (left) beam. The position of each beam at the detector focal plane can be controlled using translation stages in either arm of the beam combiner.

During the initial stages of combining the beams, it is advantageous to keep the two beams spatially separate at the detector plane in order to independently calibrate and tune each AO system. Figure 1 shows images of the two AO-corrected beams simultaneously acquired at two separate positions on the detector imaged in the $L'$ filter. In this case, one AO was set with 200 modes of correction and the other at 400 modes. These images match well to the diffraction limited PSF described in Esposito et al. (2011)[7] scaled to the appropriate wavelength. Both the images and the radial profile measurements demonstrate the dramatic improvement when increasing from 200 to 400 modes of AO correction. In particular, the performance between 0.75″ and 1.2″ improves remarkably, with a significant reduction in the residual seeing disk.

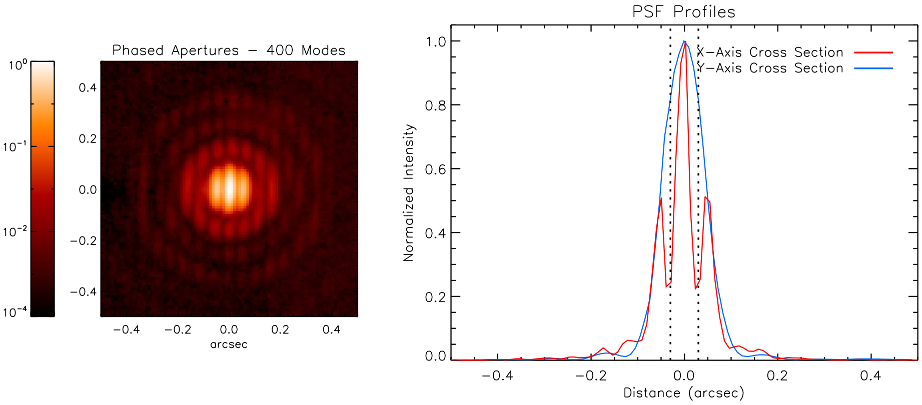

Figure 3. *Left*: Median-combined image of 50 hand-picked frames showing the interferometric PSF at ~4 $\mu$m with 400 modes of AO correction. The resulting Strehl ratio is ~0.9 without continuous fringe stabilization. Total integration time is ~1.5 sec. *Right*: Cross-sectional cuts through the center of the PSF along the horizontal and vertical directions. The red curve shows the fringed Fizeau PSF along the horizontal direction while the blue curve shows the classical Airy pattern PSF along the vertical direction. The vertical dotted lines correspond to a distance of 30 mas.

Downloaded From: http://proceedings.spiedigitallibrary.org/ on 02/01/2013 Terms of Use: http://spiedl.org/terms

Once the two PSFs are tuned, they are overlapped on the detector by adjusting two translation stages within the beam combiner. In order to produce interferometric fringes, delay lines are then adjusted such that the two beams are coherently combined and produce the characteristic diffraction pattern along the direction of the fixed two-telescope baseline. As of this writing, this can only be accomplished manually by monitoring the fringe pattern at the desired wavelength (either in imaging or spectroscopic mode). Stabilizing the fringe pattern requires a fast path-length corrector in order to correct for atmospheric and other environmental disturbances that may affect the path-length difference of the two beams. As part of the baseline LBTI design, an automatic closed-loop fringe-tracker within NIC disperses $K$-band light and uses the dispersed fringes to constantly monitor and adjust the lengths of the beam paths. Figure 2 shows a time series of twelve images monitoring the stability of the interferometric PSF over a period of approximately three seconds. Figure 3 displays a median-combined image of 50 of the best frames from a time series of 1000 unsaturated images observed at $\lambda \sim 4$ $\mu$m. The first null positions are located approximately 30 mas from the center of the PSF core, consistent with the expected relation $\theta = \frac{\lambda}{2D}$, where $D$ is the separation between the two mirrors (14.4 meters).

### 2.2 Grism Spectroscopy

Two different germanium grisms have been diamond fly cut for LMIRcam by Lawrence Livermore National Laboratory (LLNL).[8] The first has a groove density of 40 lines/mm and blaze angle of 2.8 deg. It provides $L$-band spectroscopy with first order peak efficiency at 3.6 $\mu$m. The second has a groove density of 32 lines/mm and also blaze angle of 2.8 deg. It provides $M$-band spectroscopy with first order peak efficiency at 4.4 $\mu$m and also $K$-band spectroscopy with second order peak efficiency at 2.3 $\mu$m. Anticipated spectral resolution is of order $R = 300$.

For each grism, two copies have been manufactured in order to orient the dispersion direction either parallel or perpendicular to the fringe pattern. The slit width is then matched to the spatial resolution along the given orientation. For instance, a slit aligned along the fringes with a width of 60 mas will produce higher resolution spectra with a slight trade-off in flux as compared to a perpendicular slit matched to the resolution of a classical Airy pattern.

Initial tests in March 2012 consisted of uncoated grisms using the internal NIC light source as well as sources on the sky. Anti-reflection coatings will be applied to both entrance and exit surfaces of the grisms in the summer of 2012. The grisms mount in a filter wheel just upstream of the detector at a location adjacent to an image of

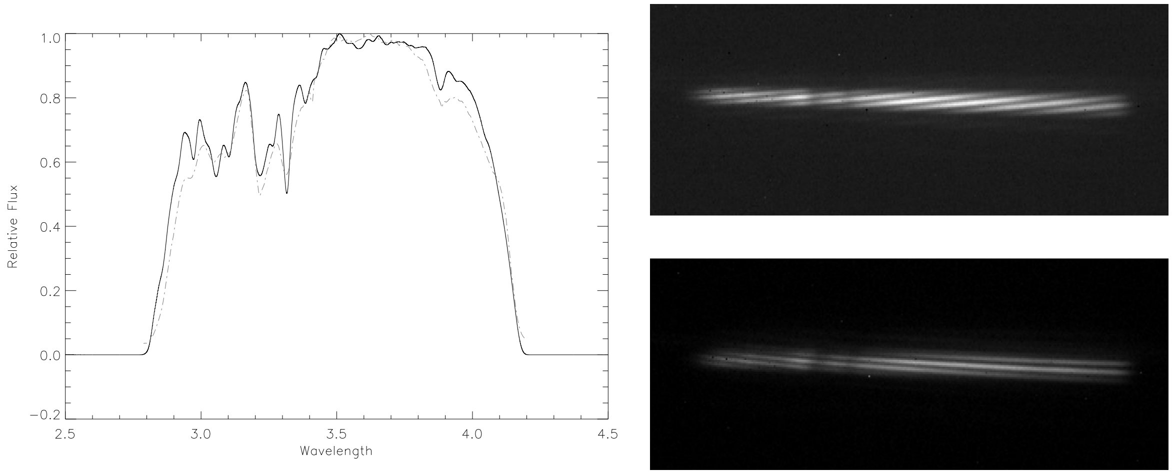

Figure 4. *Left:* Extraction of a single nod-subtracted frame of the bright star HD 82198 observed with slitless spectroscopy (dot-dashed gray curve) as compared to atmospheric transmission model multiplied by the modeled $L$-band grism efficiency curve, a order sorting filter transmission, and the dichroic transmission (solid black curve). *Right:* Images showing the the interfered light spectrally dispersed from $2.8 - 4.1$ $\mu$m at two different path length settings.

Downloaded From: http://proceedings.spiedigitallibrary.org/ on 02/01/2013 Terms of Use: http://spiedl.org/terms

the instrument Lyot stop. While a grism is used in converging light, it is a slow beam: f/16 envelope for the coherently combined light.

Even though LMIRcam is currently deployed with slits, initial on-sky tests were conducted in slit-less mode such that the spectral resolution is defined by the FWHM of the AO-corrected PSF's. The left panel of Figure 4 shows a preliminary extraction of nod-subtracted fringes of the bright star HD 82198 dispersed by the $L$-band grism. The spectra is simply from a 29 msec integration of the coherently combined light from the AO-corrected telescope apertures. The extraction (median combination of 20 pixels across the fringes), shifted and scaled by-eye, compares well to the ATRAN $L$-band atmospheric transmission model[9] for 1.5 airmasses and 1.0 mm precipitable water vapor (available from the Gemini Observatory website) multiplied by LMIRcam's optical transmission.

On-sky observations also showed that the dispersed light from the grisms can be used to fine tune the phasing between apertures. The right panel of Figure 4 gives examples of dispersed for two separate path length adjustments.

## 2.3 Apodized Phase Plates

The Apodized Phase Plate (APP) coronagraph is a realization of Phase Apodization Coronagraphy theory developed by John Codona at the University of Arizona.[10] It differs from many other currently implemented coronagraphs in that there is no occulting mask or optic in the first imaged focal plane. Instead, the pupil wavefront phase is modified at the intermediate pupil plane of LMIRCam, resulting in a PSF with diffraction suppressed over a 180 degree zone on one side of the Airy core. The highly aspheric phase pattern is introduced by varying the thickness of a transmissive optical material (Zinc Selenide) produced with a diamond turning process. APPs are chromatic with maximum suppression centered within the $L$-band at 4.08 $\mu$m. The coronagraph is completely insensitive to vibrations and tip-tilt errors in the adaptive optics system. In addition, there is no overhead in going from direct to APP observations so one can carry out typical infrared beamswitching strategies. The APP coronagraph has been demonstrated on both the MMTO telescope[11] and on the VLT, successfully imaging the planet beta Pictoris b.[12]

There are four APP optics, one pair producing an upward facing region of suppression in each aperture, and another pair producing a downward facing region of suppression, enabling full 360 degree of coverage around the target star. The suppression is from 2 to 9 $\lambda/D$ (0.18 to 0.81″) centered in the $L$-band atmospheric window.

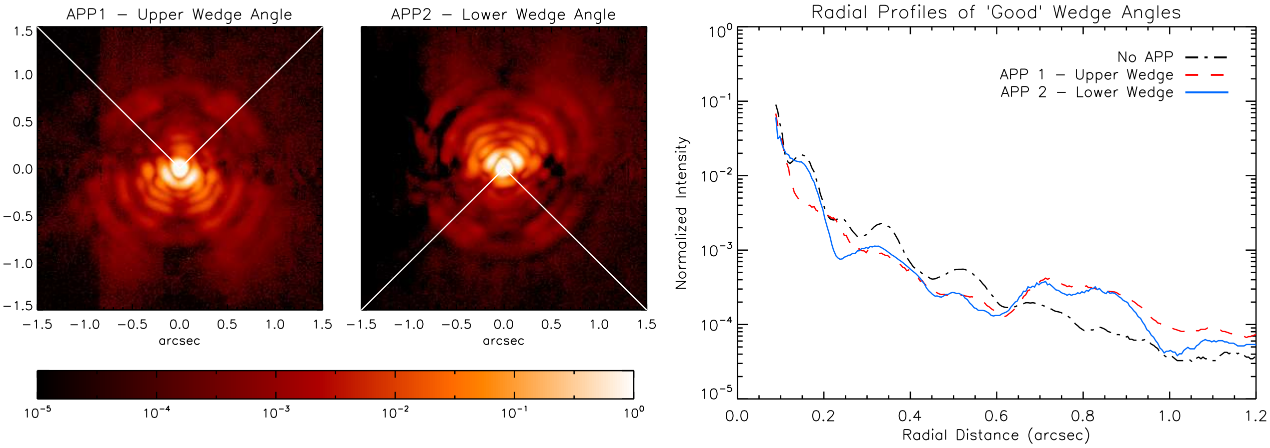

Figure 5. *Left*: Preliminary images of two APPs in similar fashion to Figure 1. Adaptive optics were in closed loop with 400 modes of correction. Each plate was designed such that the 'good' regions are opposite each other, as indicated by the white lines overplotted on the images. Two copies of a given orientation exist such that one plate covers each LBTI aperture; however, only one of each is shown here. *Right*: Radial profile plots taken within a wedged region of the APPs as compared to the radial profile of the on-sky 400-mode case from Figure 1. The APPs succeed in reducing the brightness of the PSF within these wedged regions, thereby removing residual speckle noise and increasing the effective contrast shortward of 0.7″. Any deviation between the two APPs is likely due to slight differences in the manufacturing of the individual pieces.

Downloaded From: http://proceedings.spiedigitallibrary.org/ on 02/01/2013 Terms of Use: http://spiedl.org/terms

They can be used to image both apertures individually, or combined to provide the full 22.8-meter PSF. The main benefit of combining the individual apertures is to increase the flux of a candidate planet and minimize noise.

The LMIRCam APP optics were manufactured by II-VI and are a Zinc Selenide substrate with a gold mask coating to mask out the edge of the telescope pupil. Data from both telescope apertures and both pairs of APP directions was obtained on 14 April 2012, for a total integration of 120 seconds for each APP. A logarithmic image of the APP PSFs are shown in Figure 5 along with a radial cut of the resultant PSF profile. The profile is consistent with the theoretical APP PSF profile combined with an uncorrected halo from the adaptive optics system, dominated by the time lag residuals. The goal is to produce 12 magnitudes of contrast at $2.5\lambda/D$ $(0.23'')$ for two hours of on-sky integration.

## 2.4 Non-Redundant Masking

Non-redundant masking (NRM) works by turning a single large aperture (or two large apertures in the case of LBTI) into a many-element Fizeau interferometer. The mask produces non-redundant baseline separations among apertures, and the power measured at certain spatial frequencies and position angles can be equated with pairs of sub-apertures in the mask, providing a method to measure the Fourier amplitudes and phases for each of the baselines. Because the atmosphere corrupts the measured phases, one must rely on closure phases, which are the sums of phases around triangles of sub-apertures. Closure phases are independent of atmospheric effects

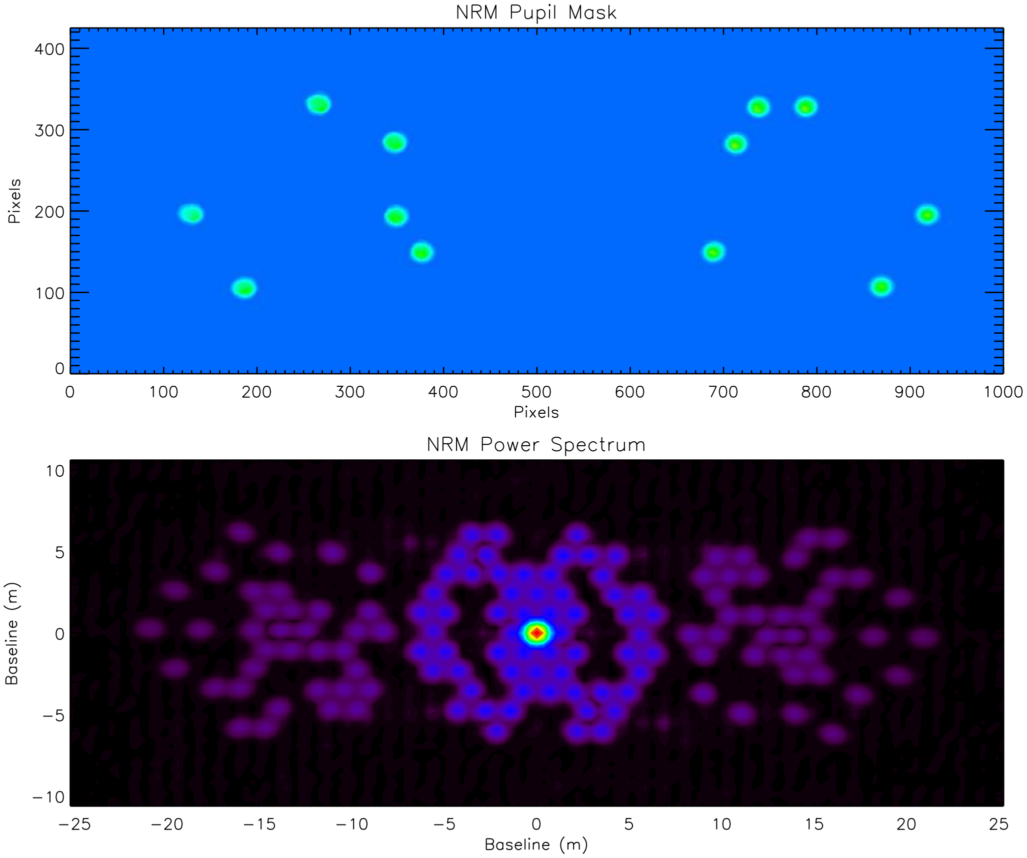

Figure 6. *Top*: Image of the 12-hole NRM mask placed at the pupil plane as observed by LMIRcam using the pupil imaging lens. The separate six-hole clusters correspond to the two telescopes of the LBT. *Bottom*: Observed power spectrum of a bright calibrator obtained during LMIRCam observations from May 2012, corresponding to the above 12-hole mask. The central cluster of points corresponds to baselines up to 8-m lying within individual LBT apertures. The left and right clusters correspond to the long baselines up to the edge-to-edge separation of the LBTI.

Downloaded From: http://proceedings.spiedigitallibrary.org/ on 02/01/2013 Terms of Use: http://spiedl.org/terms

and so provide intrinsic phase information about the source. NRM allows precise calibration of amplitudes and closure phases, and recovery of information from within the diffraction limit of the telescope.

Non-redundant masking achieves high precision at the expense of reduced throughput. Different masks are optimized for either throughput (a 12-hole mask), Fourier coverage (a 24-hole mask), or both at the expense of calibration precision (a partially redundant dual-annulus mask). We will use NRM with the two LBT AO systems and a phase tracker to co-phase both apertures. The use of non-redundant masking down-stream of an AO system has significant advantages.[13] While the mask improves the calibration of the PSF and enables super-resolved imaging, the AO system improves the coherence length and time over atmospheric limits. Thus, masks behind an AO system can use larger sub-apertures and remain diffraction-limited. Furthermore, longer integration times can be used. Both of these effects mean that AO+masking is more sensitive than masking alone. NRM observations with LMIRcam are anticipated to provide >7 mags of contrast from $\sim 0.5 - 4\ \lambda/D$ ($0.04$ to $0.36''$ in $L'$).

## 3. ELECTRONICS

### 3.1 Detector Configuration

LMIRcam was originally envisioned to operate a Teledyne Imaging Sensors HAWAII-1RG (HgCdTe Astronomy Wide Area Infrared Imager with 1024×1204 pixels, Reference pixels and Guide mode; H1RG) detector with a wavelength cutoff of $\sim$5.3 $\mu$m at the instrument focal plane during first-light operations. The HAWAII-1RG multiplexer offered up to 16 parallel output channels divided into 16 contiguous regions of 64×1024 pixels. Under normal clocking conditions, the detector runs in either a Slow or Fast mode with maximum pixel rates of 100 kHz and 5 MHz, respectively. These two modes represent a trade-off between pixel rate and read noise with the slower data rate providing the lowest read noise and the faster data rate increasing read noise by approximately five to ten times.

The HAWAII-1RG failed mechanically prior to first light on the LBT and has since been replaced with a 2048×2048 HAWAII-2RG (H2RG). This detector is electronically equivalent to the H1RG, with the exception of the larger array size and 32 readout channels. Given the original format of the HAWAII-1RG, the readout electronics for LMIRcam consists of a FGPA-based "FORCAST" controller developed by Cornell University. These electronics support up to 16 channels and a readout of $1024^2$ pixels, limiting the final readout to 1/4 of the total H2RG size. The array fanout board and clocking table have been modified in order to sample the pixels in the center of the focal plane.

### 3.2 Electronic Pickup Noise

Designed to operate between $3 - 5$ $\mu$m, Poisson noise from the thermal background tends to dominate over LMIRcam's H2RG noise characteristics. However, for observations obtained in the current configuration, a substantial amount of high-frequency electronic pickup noise occurs within the raw image with a RMS of $\sim$30 ADU, which is common to all channels. This noise is observed to decrease by a factor of $\sim$3 when the filter wheel motor controllers are powered off. Fortunately, because corresponding pixels within all channels are collected simultaneously, common mode noise rejection techniques can mitigate these issues:

- **Median Subtraction** – By taking the median of the corresponding pixels within each channel, one can obtain an estimate of the pattern noise. However, issues associated with small-number statistics arise due to the fact that each calculation of the median only utilizes 16 values. Because the sample population is small, a significant uncertainty still exists within the final estimation. This uncertainty propagates when trying to determine other array characteristics such as read noise. In addition, by subtracting discrete median values, a disproportionate number of pixels may have values at or around the center of the distribution. For instance, for a channel with exemplary noise characteristics as compared to the ensemble, this channel's pixels will be statistically more likely to be chosen as the median than a channel with poor noise performance. This effect can be alleviated by calculating the median for a given channel using the other 15 channels. A sigma-clipped mean to remove bad pixel outliers could also help, but is still subject to uncertainties from small-number statistics.

Downloaded From: http://proceedings.spiedigitallibrary.org/ on 02/01/2013 Terms of Use: http://spiedl.org/terms

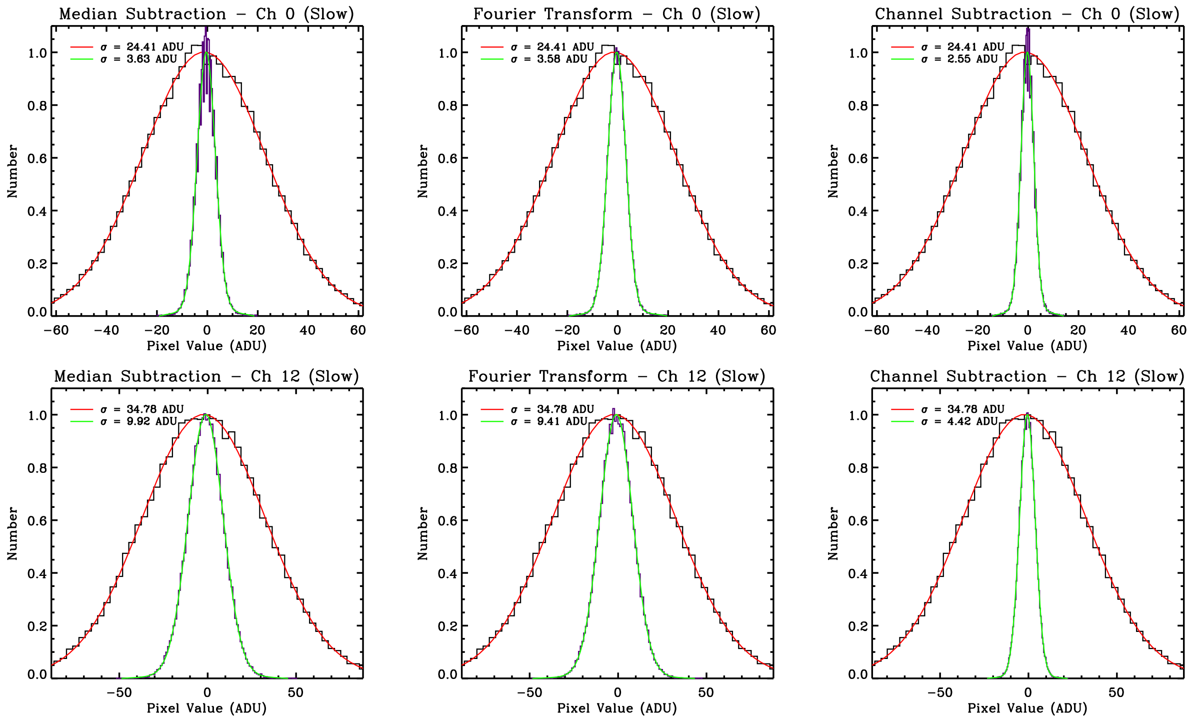

Figure 7. Comparison of three methods for removing fixed pattern pickup noise from the preamp channels while running the H2RG detector in Slow mode. Each figure presents a plot of the normalized distribution of pixels for a pair of subtracted CDS dark frames prior to any pickup noise corrections with a Gaussian fit to determine the width of the distribution. The three correction methods are then applied and compared to the original distribution. The top three plots correspond to a relatively clean channel with minimal preamp noise, while the bottom figures are for a relatively noisy channel.

- **Fast Fourier Transform** – By employing a Fast Fourier Transform (FFT), high frequency spatial noise with amplitudes above the Poisson noise can be extracted to identify and remove pattern noise common to all output channels. This method is limited by other noise sources, especially for already processed images (such as coadded and/or background-subtracted frames) that have increased uncertainties from photon noise and read noise while simultaneously smoothing out the pattern noise level (but not necessarily its influence on pixel uncertainties).
- **Channel Subtraction** – Perhaps the most accurate way to remove pickup noise from a given channel is to simply subtract any other channel within the same image, because these channels contains the exact same pickup noise pattern. This has limited implementation for science observations, though, especially for extended sources. In the future, it may be useful to machine a cold field stop that blocks one of the channels on the left and/or right of the field to use as a reference channel. In addition, these detectors provide a separate reference channel to monitor noise common to all detector channels, which would require a modification to the current fanout board.
- **Modeling the Time Domain** – Future implementation of the pickup noise removal will take into account the detector's pixel clocking code. By modeling the pattern noise for a single frame, the spatial pixel data can be visualized in the time domain, and the mean/median periodic variations common to all channels can then be fit with the noise model and subsequently removed from the data. The matter becomes somewhat more complicated with coadded data, because the pickup noise becomes a combination of multiple waves at a given frequency, but offset from each other. A Fourier transform of the time series data into frequency space should provide information on the pattern noise; however, as the pattern noise gets smoothed out, the frequency information becomes less prominent compared to other noise sources

Downloaded From: http://proceedings.spiedigitallibrary.org/ on 02/01/2013 Terms of Use: http://spiedl.org/terms

such as Poisson and read noise. Time resolution and pixel integration time also play a large role in resolving the pattern noise. Because the contamination appears to be relatively high frequency, Fast mode observations running at 5 MHz pixel rate would produce better characterization of the noise in the time domain than Slow mode observations at 100 kHz.

Figure 7 compares the histograms of the first three pickup noise removal methods with that of no pickup noise removal. All methods significantly reduce the measured noise with the channel-subtraction method consistently providing improved results over either the median-subtraction or FFT noise removal methods, especially for relatively noisy channels. Unfortunately, the channel-subtraction method is only useful for a limited number of applications when working with on-sky observations. Ideally, reading out the H2RG's separate reference channel would allow for simultaneous monitoring and removal of the pattern noise.

### 3.3 Dark Current & Pixel Operability

Dark current arises when thermal excitation within the crystal lattice of the HgCdTe layer exceeds the bandgap energy and stimulates an electron. For similar operating conditions, dark current has been measured to $<0.01$ $e^{-}$/sec/pixel for such devices.[14, 15] However, the current detector on loan from TIS is plagued with a large cluster of high dark current pixels due to a design flaw in the barrier layer of the pixel interconnect structure[a]. Essentially, an inadequate barrier between the indium bump bonds and gold contact pads within a pixel structure can cause diffusion of the gold and indium, resulting in the formation of In-Au intermetallics. Depending on the severity of the problem, which largely depends on the storage temperature of the detector, this diffusion can reach or even breach the HgCdTe crystalline layer. Such a dramatic breakdown in the pixel substructure can produce significant charge traps within the semiconductor band gap as well the production of excessive dark current.

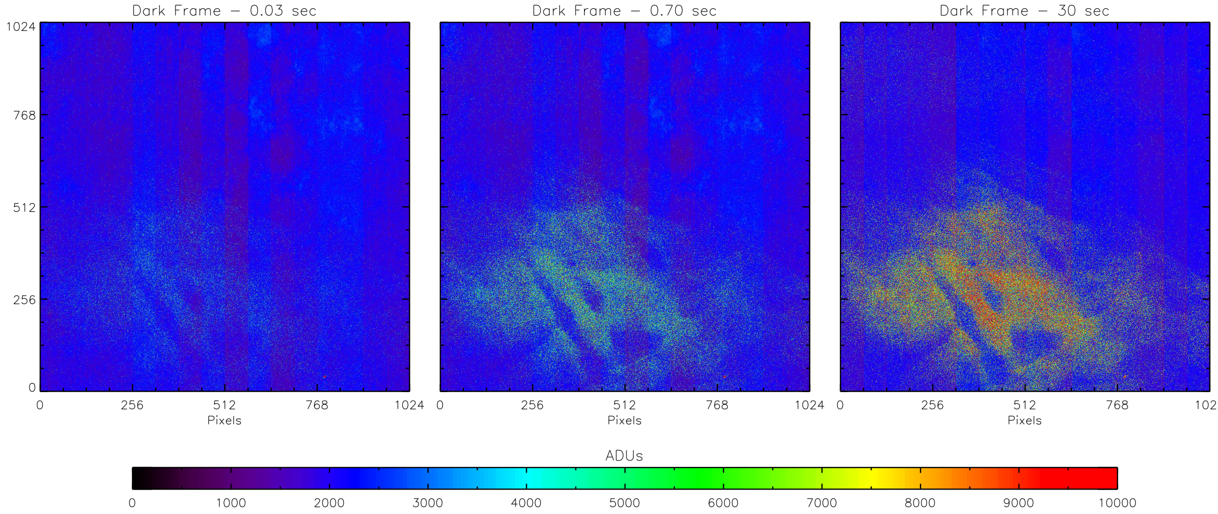

Figure 8. A set of three raw dark frames at different integration times showing the dramatic signal increase due to high dark current for a large cluster of pixels. The first two frames were acquired in Fast mode, while the image on the right was acquired in Slow mode. Detector operating temperature was set to 56K.

Figure 8 shows the spatial distribution of high dark current pixels within LMIRcam's 1024×1024 readout region[b]. A large swath of approximately $\sim 10^5$ pixels at the center of the focal plane (or 10% of the pixels in this region) exhibit abnormally high dark current signals: strong evidence for the formation of In-Au intermetallics.

---

[a] See the JWST Detector Degradation Failure Review Board Executive Summary: Root Cause Determination (http://www.jwst.nasa.gov/resources/017457.PDF)

[b] While the current data set is useful for finding the most obviously deviant pixels, extremely long exposure times are necessary in order to measure the dark current values on the order of 0.01 $e^{-}$/sec/pixel with adequate signal-to-noise. For instance, assuming a typical read noise value of 10 $e^{-}$, then approximately one hour of integration is necessary to analyze each individual pixel at S/N$\sim$5, assuming negligible thermal emission from the surrounding region.

Downloaded From: http://proceedings.spiedigitallibrary.org/ on 02/01/2013 Terms of Use: http://spiedl.org/terms

For a science-grade H2RG, dark current levels are a negligible source of noise, especially considering the large thermal background within LMIRcam's operating wavelength. Even with the current array, dithering techniques and short exposure times can mitigate effects from the large number of high dark current pixels. Regardless, the $1024^2$ readout region has been shifted upwards on the array subsequent to the this analysis in order to avoid the cluster of anomalously high dark current pixels.

### 3.4 Conversion Gain

The conversion gain is determined by applying the photon transfer method[16] to on-sky flat-field observations dominated by Poisson noise within the detector's linear regime. Multiple pairs of dark-subtracted observation are summed and differenced each frame pair. The variance is calculated from the differenced frames after correcting for pickup noise using the channel-subtraction method. The median values of the summed frames provides a measure of the signal.

Multiple effects exist that can have a significant impact on the measured system gain, including detector temperature changes over the observing time period; bias voltage drifts due to changes in external controller temperature; differing noise characteristics of the controller preamplifiers; non-uniform, spatial variations over the measured regions; time- and flux-dependent non-linearities; and interpixel capacitance, which can lead to an overestimate of the conversion gain by as much as 20%.[17–19] With these caveats in mind, the conversion gain is $g_{fast} = 8.9$ e$^-$/ADU and $g_{slow} = 8.5$ e$^-$/ADU for Fast and Slow mode, respectively. The 0.4 e$^-$/ADU difference is consistent with an expected 10% variation between Fast and Slow mode.

### 3.5 Read Noise

Upon reset of the detector array, each pixel value is initially set to some bias level, which is determined from the thermodynamic fluctuation of the number of electrons within a capacitor connected to a circuit. Referred to as reset or kTC noise, this bias value is known to have a standard deviation between 50 and 200 electrons.[15] Acquiring a correlated double sample (CDS), where a frame is non-destructively sampled at the beginning and end of exposure, removes the reset noise, which is typically greater than the pixel readout noise for a CDS acquisition.

Fowler sampling is a simple variant of CDS for improving read noise. Because the signal is read non-destructively, multiple successive samples towards the beginning and end of an exposure can be averaged to reduce the measured read noise. The effective exposure time is then the difference between the first sample of the initial group and the first sample of the final group. Theoretically, the effective total read noise is reduced by $\sqrt{N}$, where $N$ is the number of Fowler samples in each group. In the event of a non-negligble amount of flux or dark current, the noise variance per pixel of the differenced Fowler frames is

$$\sigma^2_{\rm tot} = f t_{\rm exp} - \frac{(2N-1)(N-1)}{3N} f t_{\rm frame} + \frac{\sigma^2_{\rm CDS}}{N}, \tag{1}$$

where $f$ is the flux per pixel, $t_{\rm exp}$ is the effective exposure time, $t_{\rm frame}$ is the time between successive Fowler samples within a group, and $\sigma_{\rm CDS}$ is the CDS read noise.[18] In a situation such that the flux per pixel is negligible compared to the read noise (i.e., dark frames), then the read noise per individual exposure is simply

$$\sigma_{read} = \sigma_{\rm CDS}/\sqrt{2}. \tag{2}$$

For typical LMIRcam on-sky images, the photon noise of the thermal background in the $L$ and $M$ bands dominates over read noise.

For both Fast and Slow operating modes, we acquired multiple single, CDS, and Fowler dark frames with the minimum possible exposure time in order to measure read noise characteristics (Table 3). The pattern pickup noise evident in these observations was removed using the channel-subtraction method described in Section 3.2. The total frame noise for each setup was measured by differencing two similar frames and analyzing the resulting pixel distribution. To calculate the final frame noise, a Gaussian was fit to the distribution of pixel values after discarding those pixels showing high dark current characteristics (Section 3.3). The standard deviation of the Gaussian is then divided by a factor of two in order to account for the subtraction of two frames as well as the

Downloaded From: http://proceedings.spiedigitallibrary.org/ on 02/01/2013 Terms of Use: http://spiedl.org/terms

**Table 3. Read Noise Measurements**

| | Fast Mode | | | Slow Mode | | |
|---|---|---|---|---|---|---|
| **Frame Type** | **Int. Time (sec)** | **Noise (ADU)** | **Noise ($e^-$)** | **Int. Time (sec)** | **Noise (ADU)** | **Noise ($e^-$)** |
| Single | 0.029 | 8.20 | 73.0 | 0.717 | 5.22 | 44.4 |
| CDS | 0.029 | 9.30 | 82.8 | 0.717 | 3.51 | 29.8 |
| Fowler-2 | 0.058 | 7.07 | 62.9 | 1.434 | 2.50 | 21.3 |
| Fowler-4 | 0.116 | 5.13 | 45.7 | 2.867 | 1.91 | 16.2 |
| Fowler-8 | 0.233 | 3.80 | 33.8 | 5.734 | 1.37 | 11.6 |
| Fowler-16 | 0.466 | 2.78 | 24.7 | 11.47 | 1.09 | 9.3 |
| Fowler-32 | 0.932 | 2.07 | 18.4 | 22.94 | 0.98 | 8.3 |

channel subtraction to remove the pickup noise ($\sqrt{2} \times \sqrt{2}$). The resulting CDS read noise is 82.8 and 29.8 $e^-$for Fast and Slow mode, respectively. Figure 9 plots the reduction in read noise with increasing Fowler samples.

Assuming that the dominate noise source within these CDS observations is read noise, then the kTC noise for a single frame readout can then be measured. For observations of individual frames, the measured standard deviation is approximately 73 and 44 $e^-$in Fast and Slow mode, respectively. Assuming that read noise for a single frame from follows Equation 2, then reset noise is approximately 40 $e^-$.

For Fast mode observations, the measured noise for CDS frames appears larger than for an unprocessed individual frame. This occurs because Fast mode read noise dominates over the kTC reset noise. Thus, the extra read frame for CDS observations produces more noise than the kTC noise inherent in a single-sampled frame.

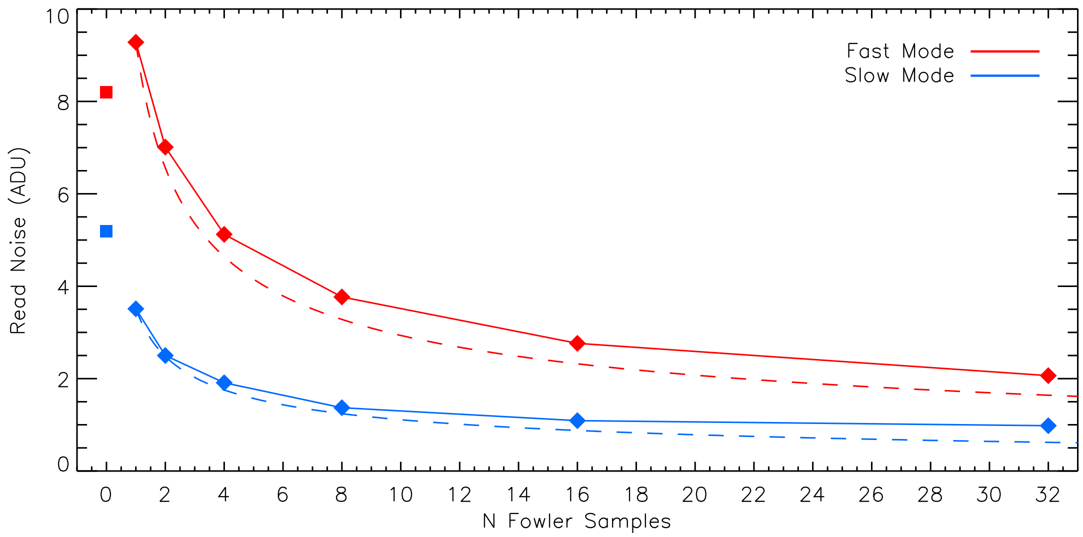

Figure 9. Plots comparing the measured read noise in ADU for Fast and Slow mode operations (Table 3). The solid lines and diamond symbols represent the measured read noise of CDS and Fowler observations, while the dashed lines indicate the theoretical $\sqrt{N}$ limit. The separate square symbols at $x = 0$ represent the total measured noise for single-frame observations.

Downloaded From: http://proceedings.spiedigitallibrary.org/ on 02/01/2013 Terms of Use: http://spiedl.org/terms

### 3.6 Well Capacity

The well capacity measures the amount of electrons able to accumulate within a detector pixel before saturating. We determine the H2RG's well capacity by sampling the detector non-destructively as it integrates over time until the frame saturates. The detector was operated in slow mode at an ambient temperature of 56 K with a light source illuminating the entire field of view. For each frame, the median of the reference pixels channel-by-channel is subtracted, then take the median of the sigma-clipped active region (for the entire frame). We then apply a linear fit to the ramp (left plot of Figure 10). The well capacity is then the point at which the linear fit deviates by 5% from the measured slope. However, the overall measured slope is inherently non-linear from start to finish and the 'correct' linear fit can be subjective. Fitting the points less than 20 seconds provides a measured well capacity of 7,850 ADU, or ∼67,000 electrons.

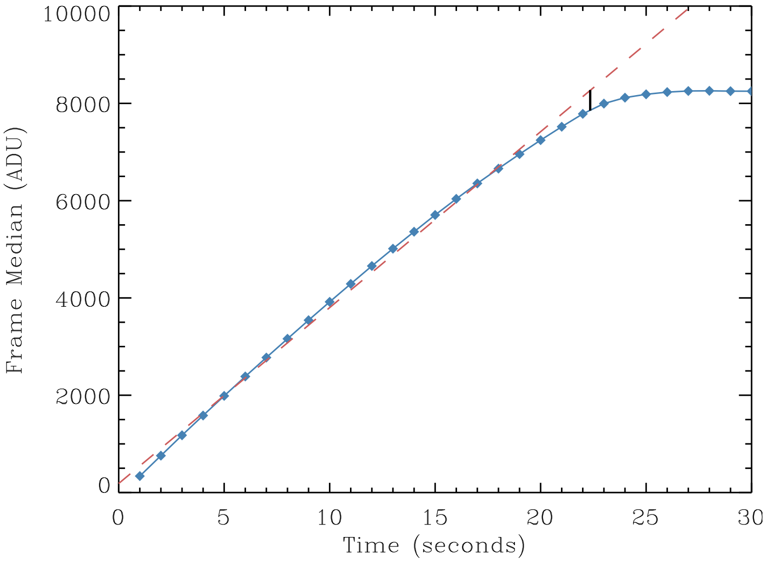

Figure 10. Plot of detector linearity over time. The blue curve shows the up-the-ramp sampled data while the red dotted lines is the best linear fit. The vertical black line indicates the point at which the sampled data deviates from the linear fit by 5%. The median of the reference pixel values have been subtracted to remove the level offsets.

## 4. SCIENCE RESULTS

Taking advantage of the LBT's uniquely powerful AO system, LMIRcam has already made significant contributions to the scientific community while operating the instrument in single-aperture imaging mode. In this section, we discuss a few projects based on LMIRcam observations in order to highlight the some of the unique features of this instrument that have been enabled through the LBT infrastructure.

- **HR 8799 Planets** – In concert with LBT-PISCES at *H*-band, Skemer et al. (2012)[20] use LMIRcam at 3.3 $\mu$m to explore the atmospheric chemistry of the four planetary-mass companions orbiting HR 8799. LMIRcam was the first instrument capable of imaging all four HR 8799 planets at this wavelength with sufficient signal-to-noise to test the atmospheric abundances of CO and $CH_4$. Combined with NIR photometry, these measurements indicate that the planets are consistently brighter at 3.3 $\mu$m than expected from equilibrium chemistry models, which predict that the opacity of $CH_4$ should produce deep absorption bands at this wavelength. Furthermore, non-equilibrium chemistry models have a difficult time fully explaining the observed SED. Instead, mixtures of cloudy atmospheres arising from a non-uniform opacity structure, similar to Jupiter's patchy atmosphere, could potentially explain the observations.

Downloaded From: http://proceedings.spiedigitallibrary.org/ on 02/01/2013 Terms of Use: http://spiedl.org/terms

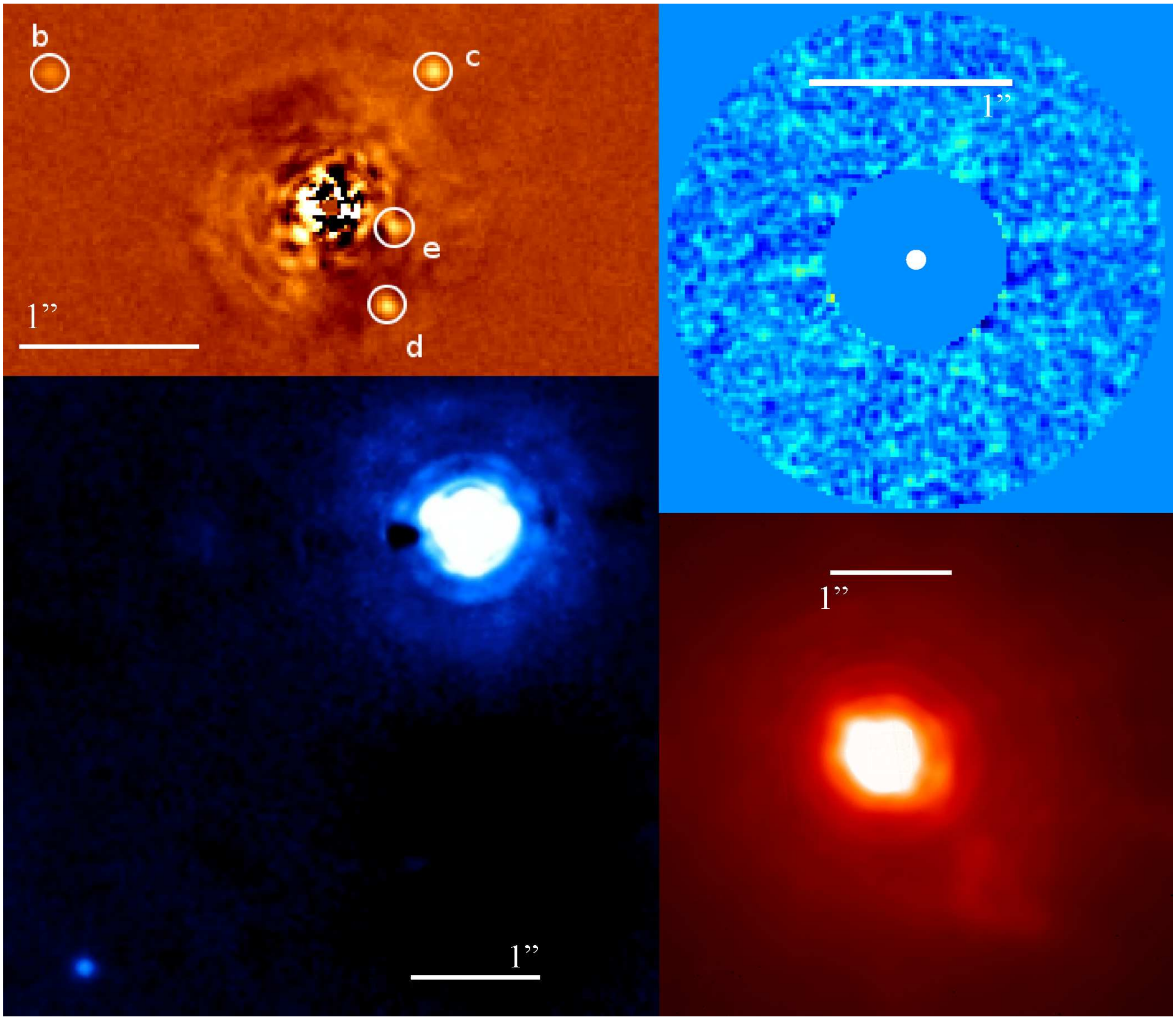

Figure 11. *Upper Left:* From Skemer et al. (2012),[20] LMIRCam image of the four HR 8799 planets at 3.3 $\mu$m, where cool exoplanets are expected to be faint, due to methane absorption. Instead, the planets were found to be much brighter than model predictions, implying the presence of non-equilibrium chemistry and/or non-isotropic cloud structures. *Upper Right:* From Rodigas et al. (2012),[21] LMIRCam image of HD 15115 showing scattered light at 3.8 $\mu$m. The fact that the debris disk is visible at such a long wavelength is the result of its composition of large dust grains. *Lower Left:* From Bailey et al. (submitted), LMIRCam image of HIP 78530 and its brown dwarf companion. LMIRCam photometry was used to look for disks around young brown dwarf companions in Upper Sco. *Lower Right:* From Shenoy et al. (in prep.), LMIRcam $M$-Band image of VY CMa. The central star is saturated to bring out the fainter nebulosity near the star. The triangular emission about $1''$ towards the southwest is know as the 'SW Clump' from HST R band images[22] and was shown to be optically thick, but still highly polarized in scattered light.[23]

- **HD 15115 Debris Disk** – Rodigas et al. (2012)[21] present scattered light images of the nearly edge-on debris disk surrounding HD 15115 observed with LMIRcam at $L'$-band as well as LBT-PISCES at $K_s$-band. Despite the relative faintness of the disk at $L'$, the is detected at 2.5$\sigma$ with a median surface brightness of $\sim$14.5 mags/arcsec$^2$. The disk surface brightness is observed to decrease interior to $1''$ at both $K_s$ and $L'$, supporting the theory of a disk gap. Furthermore, an asymmetry is detected between

Downloaded From: http://proceedings.spiedigitallibrary.org/ on 02/01/2013 Terms of Use: http://spiedl.org/terms

the two sides of the disk at $K_s$, but not $L'$. These observations suggest that scattered light from the east side of the disk originates from large dust grains, while smaller dust grains dominate the scattered light from the west side.

- **Upper Sco Companion Disks** – $L'$ and $M$-band observations of three low-mass brown dwarf companions were used to search for evidence of disks (circumstellar or substellar) within these systems (Bailey et al. 2012, submitted). Combined with NIR and 24 $\mu$m photometry, these observations provide further evidence for a disk around one of the companion stars and may be actively accreting.
- **VY CMa Dust Production** – An ultra-luminous evolved star, VY CMa is surrounded by an asymmetric nebula, $10''$ across, produced by a significantly high mass-loss rate of $4 \times 10^{-4} M_{\odot}/\mathrm{yr}$.[24] Such characteristics make VY CMa an important object for studying the process by which evolved cool stars return material to the interstellar medium. Shenoy et al. (in prep.) use LMIRcam observations to address the mass and dust properties of this source.

## ACKNOWLEDGMENTS

The National Science Foundation supported this work under Grant No. AST-0705296 at both the University of Virginia and the University of Minnesota. The LMIRcam team is grateful for the support received from the LBT organization and its partner members.

## REFERENCES

[1] Herbst, T. M., Ragazzoni, R., Eckart, A., and Weigelt, G., "The LINC-NIRVANA interferometric imager for the Large Binocular Telescope," *Proc. SPIE* **5492** (2004).

[2] Hinz, P. M., Solheid, E., Durney, O., and Hoffmann, W. F., "NIC: LBTI's nulling and imaging camera," *Proc. SPIE* **7013** (2008).

[3] Hinz, P. M., Bippert-Plymate, T., Breuninger, A., Connors, T., Duffy, B., Esposito, S., Hoffmann, W., Kim, J., Kraus, J., McMahon, T., Montoya, M., Nash, R., Durney, O., Solheid, E., Tozzi, A., and Vaitheeswaran, V., "Status of the LBT interferometer," *Proc. SPIE* **7013** (2008).

[4] Wilson, J. C., Hinz, P. M., Skrutskie, M. F., Jones, T., Solheid, E., Leisenring, J., Garnavich, P., Kenworthy, M., Nelson, M. J., and Woodward, C. E., "LMIRcam: an L/M-band imager for the LBT combined focus," *Proc. SPIE* **7013** (2008).

[5] Skrutskie, M. F., Jones, T., Hinz, P. M., Garnavic, P., Wilson, J. C., Nelson, M. J., Solheid, E., Durney, O., Hoffmann, W. F., Vaitheeswaran, V., McMahon, T., Leisenring, J., and Wong, A., "LMIRcam: an L/M-band imager for the LBT combined focus," *Proc. SPIE* **7735** (2010).

[6] Hinz, P. M., Arbo, P., Bailey, V., Connors, T., Durney, O., Esposito, S., Hoffmann, W., F., Jones, T. J., Leisenring, J. M., Montoya, M., Nash, R., Nelson, M. J., McMahon, T., Pinna, E., Puglisi, A., Skemer, A., Skrutskie, M. F., and Vaitheeswaran, V., "On-sky testing of the lbt interferometer: steps toward routine ao-stabilized interferometric observations," *Proc. SPIE* **8445** (2012).

[7] Esposito, S., Riccardi, A., Pinna, E., Puglisi, A., Quirós-Pacheco, F., Arcidiacono, C., Xompero, M., Briguglio, R., Agapito, G., Busoni, L., Fini, L., Argomedo, J., Gherardi, A., Brusa, G., Miller, D., Guerra, J. C., Stefanini, P., and Salinari, P., "Large Binocular Telescope Adaptive Optics System: new achievements and perspectives in adaptive optics," *Proc. SPIE* **8149** (2011).

[8] Kuzmenko, P. J., Little, S. L., Little, L. M., Wilson, J. C., Skrutskie, M. F., Hinz, P., Leisenring, J. M., and Durney, O., "Fabrication and testing of germanium grisms for lmircam," *Proc. SPIE* **8450** (2012).

[9] Lord, S. D., "A new software tool for computing earth's atmospheric transmission of near- and far-infrared radiation," NASA Technical Memorandum 103957, NASA (1992).

[10] Codona, J., "Phase Apodization Coronagraphy," in [*In the Spirit of Bernard Lyot: The Direct Detection of Planets and Circumstellar Disks in the 21st Century*], 24 (June 2007).

[11] Kenworthy, M. A., Codona, J. L., Hinz, P. M., Angel, J. R. P., Heinze, A., and Sivanandam, S., "First On-Sky High-Contrast Imaging with an Apodizing Phase Plate," *ApJ* **660**, 762–769 (May 2007).

Downloaded From: http://proceedings.spiedigitallibrary.org/ on 02/01/2013 Terms of Use: http://spiedl.org/terms

[12] Quanz, S. P., Meyer, M. R., Kenworthy, M. A., Girard, J. H. V., Kasper, M., Lagrange, A.-M., Apai, D., Boccaletti, A., Bonnefoy, M., Chauvin, G., Hinz, P. M., and Lenzen, R., "First Results from Very Large Telescope NACO Apodizing Phase Plate: 4 $\mu$m Images of The Exoplanet $\beta$ Pictoris b," *ApJL* **722**, L49–L53 (Oct. 2010).

[13] Kraus, A. L. and Ireland, M. J., "LkCa 15: A Young Exoplanet Caught at Formation?," *ApJ* **745**, 5 (Jan. 2012).

[14] Finger, G., Dorn, R. J., Meyer, M., Mehrgan, L., Stegmeier, J., and Moorwood, A. F. M., "Performance of large-format 2Kx2K MBE grown HgCdTe Hawaii-2RG arrays for low-flux applications," *Proc. SPIE* **5499** (2004).

[15] Beletic, J. W., Blank, R., Gulbransen, D., Lee, D., Loose, M., Piquette, E. C., Sprafke, T., Tennant, W. E., Zandian, M., and Zino, J., "Teledyne Imaging Sensors: infrared imaging technologies for astronomy and civil space," *Proc. SPIE* **7021** (2008).

[16] Janesick, J. R., [*Scientific charge-coupled devices*], SPIE Optical Engineering Press, Bellingham, WA (2001).

[17] Moore, A. C., Ninkov, Z., and Forrest, W. J., "Interpixel capacitance in nondestructive focal plane arrays," *Proc. SPIE* **5167** (2004).

[18] Rauscher, B. J., Fox, O., Ferruit, P., Hill, R. J., Waczynski, A., Wen, Y., Xia-Serafino, W., Mott, B., Alexander, D., Brambora, C. K., Derro, R., Engler, C., Garrison, M. B., Johnson, T., Manthripragada, S. S., Marsh, J. M., Marshall, C., Martineau, R. J., Shakoorzadeh, K. B., Wilson, D., Roher, W. D., Smith, M., Cabelli, C., Garnett, J., Loose, M., Wong-Anglin, S., Zandian, M., Cheng, E., Ellis, T., Howe, B., Jurado, M., Lee, G., Nieznanski, J., Wallis, P., York, J., Regan, M. W., Hall, D. N. B., Hodapp, K. W., Böker, T., De Marchi, G., Jakobsen, P., and Strada, P., "Detectors for the James Webb Space Telescope Near-Infrared Spectrograph. I. Readout Mode, Noise Model, and Calibration Considerations," *PASP* **119** (2007).

[19] Fox, O., Waczynski, A., Wen, Y., Foltz, R. D., Hill, R. J., Kimble, R. A., Malumuth, E., and Rauscher, B. J., "The $^{55}$Fe x-ray energy response of mercury cadmium telluride near-infrared detector arrays," *Proc. SPIE* **7021** (2008).

[20] Skemer, A. J., Hinz, P. M., Esposito, S., Burrows, A., Leisenring, J., Skrutskie, M., Desidera, S., Mesa, D., Arcidiacono, C., Mannucci, F., Rodigas, T. J., Close, L., McCarthy, D., Kulesa, C., Agapito, G., Apai, D., Argomedo, J., Bailey, V., Boutsia, K., Briguglio, R., Brusa, G., Busoni, L., Claudi, R., Eisner, J., Fini, L., Follette, K. B., Garnavich, P., Gratton, R., Guerra, J. C., Hill, J. M., Hoffmann, W. F., Jones, T., Krejny, M., Males, J., Masciadri, E., Meyer, M. R., Miller, D. L., Morzinski, K., Nelson, M., Pinna, E., Puglisi, A., Quanz, S. P., Quiros-Pacheco, F., Riccardi, A., Stefanini, P., Vaitheeswaran, V., Wilson, J. C., and Xompero, M., "First Light LBT AO Images of HR 8799 bcde at 1.6 and 3.3 $\mu$m: New Discrepancies between Young Planets and Old Brown Dwarfs," *ApJ* **753**, 14 (July 2012).

[21] Rodigas, T. J., Hinz, P. M., Leisenring, J., Vaitheeswaran, V., Skemer, A. J., Skrutskie, M., Su, K. Y. L., Bailey, V., Schneider, G., Close, L., Mannucci, F., Esposito, S., Arcidiacono, C., Pinna, E., Argomedo, J., Agapito, G., Apai, D., Bono, G., Boutsia, K., Briguglio, R., Brusa, G., Busoni, L., Cresci, G., Currie, T., Desidera, S., Eisner, J., Falomo, R., Fini, L., Follette, K., Fontana, A., Garnavich, P., Gratton, R., Green, R., Guerra, J. C., Hill, J. M., Hoffmann, W. F., Jones, T. J., Krejny, M., Kulesa, C., Males, J., Masciadri, E., Mesa, D., McCarthy, D., Meyer, M., Miller, D., Nelson, M. J., Puglisi, A., Quiros-Pacheco, F., Riccardi, A., Sani, E., Stefanini, P., Testa, V., Wilson, J., Woodward, C. E., and Xompero, M., "The Gray Needle: Large Grains in the HD 15115 Debris Disk from LBT/PISCES/Ks and LBTI/LMIRcam/L' Adaptive Optics Imaging," *ApJ* **752**, 57 (June 2012).

[22] Humphreys, R. M., Helton, L. A., and Jones, T. J., "The Three-Dimensional Morphology of VY Canis Majoris. I. The Kinematics of the Ejecta," *AJ* **133**, 2716–2729 (June 2007).

[23] Jones, T. J., Humphreys, R. M., Helton, L. A., Gui, C., and Huang, X., "The Three-Dimensional Morphology of VY Canis Majoris. II. Polarimetry and the Line-of-Sight Distribution of the Ejecta," *AJ* **133**, 2730–2736 (June 2007).

[24] Danchi, W. C., Bester, M., Degiacomi, C. G., Greenhill, L. J., and Townes, C. H., "Characteristics of dust shells around 13 late-type stars," *AJ* **107**, 1469–1513 (Apr. 1994).

**Downloaded From: http://proceedings.spiedigitallibrary.org/ on 02/01/2013 Terms of Use: http://spiedl.org/terms**